Green Chemistry

PAPER

View Article Online
View Journal | View Issue

Cite this: *Green Chem.*, 2020, **22**, 4952

Water-based fabrication of garnet-based solid electrolyte separators for solid-state lithium batteries†

Ruijie Ye, [a,b] Chih-Long Tsai, ‡[a] Martin Ihrig, [a] Serkan Sevinc,[a] Melanie Rosen,[a] Enkhtsetseg Dashjav,[a] Yoo Jung Sohn, [a] Egbert Figgemeier*[b,c] and Martin Finsterbusch *[a,c]

Received 21st March 2020,
Accepted 16th June 2020

DOI: 10.1039/d0gc01009j

rsc.li/greenchem

Garnet-type $Li_7La_3Zr_2O_{12}$ (LLZ) is regarded as a promising oxide-based solid electrolyte (SE) for solid-state lithium batteries (SSLBs) or other advanced Li-battery concepts like Li–air or Li–S batteries. A thin free-standing LLZ sheet can be fabricated by tape-casting and used *e.g.* as separators in SSLBs, since tape casting is an industrially established process and enables large-scale production of such SEs. However, organic solvents and additives employed in conventional slurry recipes for tape-casting give rise to health and safety concerns and also cause a high cost for solvent recovery. Hence, development of a green, water-based processing route can reduce both manufacturing costs and environmental footprint. In this work, we developed a tape-casting process for LLZ SEs using water as solvent, the water-soluble biopolymer methylcellulose as binder and other eco-friendly polymers as plasticizers. Although a Li^+/H^+ exchange takes place during our procedure, we demonstrate that the Li^+/H^+ exchange reaction is reversible in our procedure and results in the formation of stoichiometric cubic LLZ at the end. The obtained free-standing LLZ sheets with thickness of 150 μm and relative density of approx. 90% offer an ionic conductivity of 0.15 mS cm^{-1} at room temperature. We thereby prove that it is feasible to use water as dispersion medium and eco-friendly polymer additives for the fabrication of thin garnet-based SE layers.

Introduction

Lithium ion batteries (LIBs) power almost all portable electronic devices, electrical vehicles and increase their market share in stationary storage applications.[1–7] However, the energy density of the conventional LIBs comprising organic liquid electrolytes will soon reach its physicochemical limit.[8] Additionally, the flammable organic electrolytes raise concerns regarding safety when cells and systems are scaled up. In contrast, solid-state lithium batteries (SSLBs) that use solid electrolytes (SEs) instead of liquid ones are becoming a promising solution for safer batteries with higher energy density.[8,9] Common materials used for SEs are oxides, sulfides and polymers. In general, the ionic conductivities of oxide and sulfide SEs are 2 to 4 orders of magnitudes higher than the ones of polymer SEs, and the oxides have higher chemical stability than sulfides in air, which enables the production and processing of oxides SEs in ambient atmosphere.[10–12] Among different solid electrolytes, the garnet-type compound $Li_7La_3Zr_2O_{12}$ (LLZ) has drawn particular attraction as a perspective solid lithium ion conductor for different battery concepts.[13–15] LLZ has a relatively high ionic conductivity of up to 10^{-3} S cm^{-1} at room temperature (r.t.) enhanced by different substitutions such as Al, Ta, Ga and Nb.[15–18] The unique feature of LLZ is its high chemical and electrochemical stability *versus* lithium metal,[19,20] which makes LLZ a very attractive SE material for the use with a metallic Li anode. Since the discovery of LLZ in 2007,[21] an intensive research was conducted to integrate LLZ in SSLBs or to use LLZ as single ion conducting separators in other post Li-ion-battery concepts such as Li–air and Li–S.[13–15] However, the progress in the development of LLZ-based electrochemical energy storage

[a]*Institute of Energy and Climate Research – Materials Synthesis and Processing (IEK-1), Forschungszentrum Jülich GmbH, 52425 Jülich, Germany. E-mail: m.finsterbusch@fz-juelich.de*
[b]*Institute for Power Electronics and Electrical Drives (ISEA), RWTH Aachen University, 52066 Aachen, Germany. E-mail: e.figgemeier@fz-juelich.de*
[c]*Helmholtz Institute Münster (IEK-12), Forschungszentrum Jülich GmbH, 48149 Münster, Germany*

†Electronic supplementary information (ESI) available: Calculation of conductivity; calculation of degree of Li^+/H^+-exchange and pH value of slurry; XRD patterns and ICP-OES results of LLZ samples from each step of the fabrication procedure; XRD pattern of Na-doped LLZ:AlTa. See DOI: 10.1039/d0gc01009j

‡Present address: Institute of Energy and Climate Research – Fundamental Electrochemistry (IEK-9), Forschungszentrum Jülich GmbH, 52425 Jülich, Germany.

devices is still slow due to the multiple challenges with the fabrication process.[22–25] Processing methods that are cheap, scalable and environmentally benign are needed to demonstrate economic feasibility of LLZ-based devices. In particular, the fabrication of dense thin layers acting as SE separators in SSLBs using scalable industrial methods still needs to be developed.

Tape casting is a well-known technique for large-scale production of free-standing ceramic components with layered structures, *e.g.* in the field of solid oxide fuel cells (SOFCs) that are usually composing more than 3 layers for a SOFC.[26–28] Large area foils of ceramic material are prepared from a slurry containing ceramic powder, dispersing agents, binders and plasticizers in a suitable solvent, which is cast in a continuous process and can be cut into desired shape and sintered at elevated temperature in a subsequent step to obtain the desired component. Recently, several researchers have reported applying this technique for the fabrication of LLZ thin layers (Table 1). Yi *et al.*[29,30] successfully fabricated ultrathin layers with a thickness less than 30 μm from Ga- and Al-doped LLZ nanopowders. Wachsman and co-workers made great efforts in fabrication of not only dense but also porous LLZ layers.[31–33] Several studies reported the using of additional sintering additives, *e.g.* Li_3BO_3,[34] ZnO,[35] Al_2O_3,[36] Li_2O[37] to achieve higher density of the LLZ tapes, which, however, can lead to the reduction of their electrochemical performances. Furthermore, the tape casting slurries in all these works used organic solvents, raising health and safety concerns and increasing the manufacturing costs due to the need of solvent recovery. Hence, the development of a green, water-based processing route that can reduce both manufacturing costs and environmental footprint are of concern. Since LLZ is known sensitive to water,[38] there are few reports on water-based processing of LLZ till now. To our knowledge, there are only two demonstrated examples in literature reporting the aqueous tape-casting of LLZ[39] and an aqueous-based gelcasting process of LLZ.[40] The reported aqueous tape-cast LLZ was found to partially decompose during sintering in air forming Zr-containing

Table 1 Examples of fabrication of garnet solid electrolytes by tape casting

Powder	Solvent	Dispersant	Binder	Plasticizer	Thickness [μm]	Sintering parameters	Ionic conductivity [mS cm^{-1}]	Ref.
$Li_{6.25}La_3Al_{0.25}Zr_2O_{12}$	Ethanol Acetone	PAA	PVB	BBP	28	1080 °C, 1 h, N_2 800 °C, 1–4 h, O_2	0.2 (r.t.)	29
$Li_{6.25}La_3Ga_{0.25}Zr_2O_{12}$	Ethanol Acetone	PAA	PVB	BBP	25	1130 °C, 0.3 h, N_2 800 °C, 1–4 h, O_2	1.3 (r.t.)	30
$Li_7La_{2.75}Ca_{0.25}Zr_{1.75}Nb_{0.25}O_{12}$	Toluene IPA	Fish oil	PVB	BBP	35 (dense) 70 (porous)	700 °C, 4 h, air 1100 °C, 6 h, air	0.22 (22 °C)	31 and 32
$Li_{6.75}La_{2.75}Ca_{0.25}Zr_{1.5}Nb_{0.5}O_{12}$	Toluene IPA	Fish oil	PVB	BBP	14 (dense) 70 (porous)	1050 °C, 1 h, air	Not mentioned	33
$Li_7La_3Al_{0.1}Zr_{1.75}Nb_{0.25}O_{12}$, Li_3BO_3	Toluene Ethanol	Fish oil	EC	PEG DBP	150–175	650 °C, 1 h, air 1000 °C, 6 h, Ar	0.283 (r.t.)	34
$Li_{6.16}La_3Al_{0.28}Zr_2O_{12}$, ZnO	Ethanol Xylene Toluene	Fish oil	PVB	PEG BBP	500	600 °C, 1 h, air 1250 °C, 5 h, air	0.08 (25 °C)	35
$Li_7La_3Zr_2O_{12}$, Al_2O_3	THF, IPA Butanol	Rhodaline	PVA PVB	Not mentioned	80–100	900 °C, 6 h, air 1200 °C, 6 h, Ar/H_2	0.1 (22 °C)	36
$Li_{6.4}La_3Zr_{1.4}Ta_{0.6}O_{12}$, Li_2O	Ethanol BuAcO	None	PAR	MB	200	650 °C, 1 h, air 1100 °C, 6 h, air	0.52 (30 °C)	37
$Li_{6.5}La_{2.8}Ga_{0.2}Zr_{1.75}Nb_{0.25}O_{12}$	Water	None	WB04B-53	None	90 (green)	800 °C, 2 h, air 1040 °C, 2 h, Ar	0.5 (r.t.)	39
$Li_{6.5}La_3Zr_{1.5}Ta_{0.5}O_{12}$	Water	None	WB4101		Not mentioned	800 °C, 2 h, air 1140 °C, 2 h, Ar	0.32 (r.t.)	39
$Li_{6.45}Al_{0.05}La_3Zr_{1.6}Ta_{0.4}O_{12}$	Water	None	MC	PEG Glycerol	150	750 °C, 1 h, air 1175 °C, 4 h, air	0.15 (r.t.)	This work

IPA: isopropanol; THF: tetrahydrofuran; BuAcO: butyl acetate; PAA: polyacrylic acid; PVB: polyvinyl butyral; PVA: polyvinyl acetate; EC: ethyl cellulose; PAR: polyacrylic resin; MC: methylcellulose; BBP: benzyl butyl phthalate; DBP: dibutyl phthalate; PEG: polyethylene glycol; MB: methyl benzoate; r.t.: room temperature.

secondary phases, which lowered the ionic conductivity by factor of two. The gel-cast SE, on the other hand, is much thicker (1 mm) than tape-cast ones and would thus decrease the energy density on cell level. Moreover, both of them applied synthetic binders and used LiOH to prevent Li^+/H^+-exchange, which complicates the process and make it more expensive. Therefore, in our study we developed a water-based tape-casting process of LLZ by using green binders and plasticizers, making it even simpler and more environmentally benign. This advancement can pave the way for scaled industrial application of high ionic conductive LLZ SEs for SSLBs and advanced Li-batteries.

The substitution of the solvent from organic to water in conventional tape-casting slurries is a good way to make the processing simpler and thus cheaper. However, to make the process even more "green" and thus further increasing the environmentally benign, the employed binders also need to undergo a green evolution (Fig. 1).[41] Polytetrafluoroethylene (PTFE) and poly(vinylidene fluoride) (PVdF) are widely used binders for electrodes that are used in supercapacitors and LIBs.[42,43] Both of them are F-containing while PVdF even requires the use of the hazardous organic solvent *N*-methyl pyrrolidone (NMP),[42] so that they do not meet the criterion of non-toxic green process. F-free Polyvinyl acetate (PVA) and polyvinyl butyral (PVB) are usually employed as binder in ethanol-based tape casting processes,[29,30,35,36] but they are still incomunitedible with aqueous processing due to their poor solubility in water. Higher water solubility is obtained for polyvinyl alcohol (PVOH) and poly(acrylic acid) (PAA) owing to the hydrophilic hydroxyl and carboxyl group, respectively.[44,45] However, the production of all these synthetic polymers highly relies on non-renewable fossil resources. One step further towards green binders is the application of bio-polymers and their derivatives that originate from sustainable resources, for instance polysaccharides. Polysaccharides are polymeric carbohydrates consisting of a large amount of monosaccharides linked glycosidically, which can be often found in form of starch, cellulose, alginate, chitosan, pectin *etc*.[41] Among them carboxymethyl cellulose (CMC) is an intensively studied bio-derived binder used in the fabrication of electrodes for LIBs.[46–48] However, the commercial CMC is usually only available in the form of its sodium salt, where the Na-containing compound can react with LLZ at elevated temperatures as shown in Fig. S3.† Therefore, it is crucial to find new bio-derived binders that are composed of only C, H and O for the manufacturing of garnet based SEs for SSLBs and advanced Li-batteries.

In this work, we developed a novel aqueous tape casting route to fabricate thin, dense, free-standing films of LLZ. All binders and additives used in here are bio-polymeric or non-toxic substances. After sintering in air and a subsequently annealing process in Ar, the obtained LLZ layers show a high ionic conductivity and enable the use of metallic Li as anode for SSLBs and other advanced Li-battery concepts. In addition, we also investigated the effect of water on LLZ during the whole procedure to prove that this developed aqueous processing route is feasible to obtain desired garnet SE with pure cubic phase with high ionic conductivity.

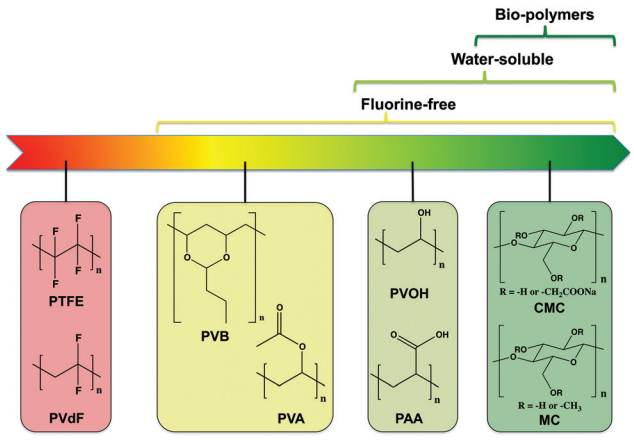

Fig. 1 Green evolution of binders.

Experimental

Garnet solid electrolyte preparation

Ta- and Al-Substituted $Li_{6.45}Al_{0.05}La_3Zr_{1.6}Ta_{0.4}O_{12}$ (LLZ:AlTa) was selected as the SE material because Ta and Al can stabilize the cubic structure of LLZ and lead to an increased ionic conductivity.[16,49] LLZ:AlTa powder was prepared *via* a four-step solid-state reaction as described in our previous work.[50] The synthesized powder corresponds to a cubic LLZ phase, as follows from the X-Ray diffraction (XRD) patterns (Fig. S1†). A small impurity phase of Li_2CO_3 detected in XRD can be attributed to the excess lithium reagent added into the synthesis process for compensating lithium loss during the whole sintering process, which is confirmed by ICP-OES giving the overall lithium concentration high than the targeting $Li_{6.45}Al_{0.05}La_3Zr_{1.6}Ta_{0.4}O_{12}$ (Table S1†). The as-prepared LLZ:AlTa powder was then milled for 60 h with 5 mm diameter ZrO_2 grinding media in isopropanol (99.5%, Alfa Aesar), followed by drying in an oven at 70 °C.

An aqueous polymer solution was prepared in advance by dissolving methylcellulose (MC, Alfa Aesar), polyethylene glycol (PEG, Merck) and glycerol (Merck, 99%) in deionized water. The ball-milled LLZ:AlTa powder was added into the polymer solution. This suspension was then homogenized under vacuum (10 kPa) with 5 mm diameter ZrO_2 beads in a planetary mixer (Thinky, USA) at 1000 rpm for 5 min to form the slurry for tape casting. The formulation of the slurry is summarized in Table 2. Afterwards, the obtained slurry was cast on a Mylar foil using a moving doctor blade. The thickness of green tapes were controlled by varying the gap of a doctor blade. After drying overnight at ambient atmosphere, the green tapes were manually peeled off the Mylar foil and cut into desired sizes. Two layers of the green tape were laminated at 80 °C with a pressure of 120 MPa for 2 min to

Table 2 Formulation of slurry for tape casting

Materials	Function	Weight percent [%]
LLZ:AlTa	Solid	52.40
deionized water	Solvent	43.66
Methylcellulose	Binder	0.44
Polyethylene glycol	Plasticizer	1.75
Glycerol	Plasticizer	1.75

improve the packing density. The laminated green tapes were punched into discs with 14 mm diameter for sintering.

The green discs were placed between two MgO plates with LLZ-coatings inside a closed alumina crucible. The crucible was heated up in air at a heating rate of 1 °C min^{-1} to 700 °C with 1 h dwell time and subsequently at a heating rate of 10 °C min^{-1} to 1175 °C with 4 h dwell time for sintering. Afterwards, the sample were free cooling to r.t. The obtained dense garnet discs were labeled as LLZ-air. Samples of LLZ-air were further placed on an alumina boat and annealed in a tube furnace with flowing argon at 800 °C with 1 h dwell time and were noted as LLZ-Ar.

Material characterization

The samples were characterized for their phase purities by XRD on a Bruker D4 Endeavor device (Bruker, Germany) using Cu Kα radiation equipped with a 1D detector LynxEye. The TOPAS V4 software (Bruker AXS) was used for Rietveld refinements to determine the lattice parameters of the samples. Raman spectroscopy was carried out with a Renishaw inVia Raman microscope using a solid-state 532 nm excitation laser and 1800 lines per mm grating. Inductively coupled plasma optical emission spectroscopy (ICP-OES) was used to determine the stoichiometry of the LLZ-Ar sample. Particle size distribution (PSD) was determined by Fraunhofer diffraction using a Horiba LA-950V2 instrument (Horiba, Japan). The viscosity of the slurry was measured by a rheometer Physica MCR100 (Anton Paar, Austria) with a cylinder DG26.7 measuring system. The thermogravimetric analysis (TG) was conducted on the thermal analyzer (Netzsch STA 449 F1 Jupiter) coupled with a mass spectroscopy (MS) (Netzsch 403 C Aeolos). For microstructural investigation on cross-section, samples were embedded in EpoFix epoxy resin (Struers, Germany) and mirror-polished. Back-scattered electron (BSE) images of the microstructure were taken by a scanning electron microscope (SEM) (TM3000 tabletop microscope, Hitachi). Density was calculated by phase analysis of the cross-sectional SEM image using the image processing software Fiji (NIH Image).

Electrochemical characterization

For electrochemical measurements, a VMP-300 multi-potentiostat (BioLogic) combined with a climate chamber (Vötsch VT4002EMC) was used. A cyclic voltammetry (CV) measurement was conducted in the potential range from −0.02 V to 5 V *vs.* Li^+/Li at a scan rate of 0.02 mV s^{-1}. The garnet solid electrolyte sample for CV measurement was sandwiched between one metallic Li foil and one In foil. Electrochemical impedance spectroscopy (EIS) was measured in the frequency range from 7 MHz to 10 mHz with an electrical field perturbation of 20 mV. A fitting of the impedance spectrum was conducted in the software ZView (Scribner). For EIS measurement, sample was sandwiched between two metallic Li foils and heated up to 300 °C to obtain a better contact at the interface. The same symmetric cell was also used to conduct the Li stripping/plating tests at 80 °C with 1 h per cycle. All these measurements were performed in Swagelok cells, which were assembled inside an Ar-filled glovebox.

Results and discussion

Tape casting of garnet solid electrolyte layers

For tape casting, a slurry comprising the milled LLZ:AlTa powder and aqueous binder system was prepared. PSD of the LLZ:AlTa powder (Fig. 2) shows a trimodal curve for the powder before ball-mill, indicating the presence of large particles or agglomerates, whereas the powder after ball-milling shows only one narrow peak with a D_{50} value of 1.17 μm and is suitable for the tape casting process. As mentioned before, the commercial CMC binder contains sodium, which might exchange with Li^+ in the structure of LLZ at elevated temperature. To avoid this uncertain effect, we choose therefore Na-free MC binder. It is also worth noting that the MC, PEG and glycerol in this aqueous binder system are all non-toxic that are often used as food additives or pharmaceutical applications due to their harmless to humans.[51] Major advantage of the aqueous slurry preparation presented here is that there is no additional organic dispersant needed, because the water itself is already good dispersant. Additionally, it is well known that the immersing of LLZ in water triggers a Li^+/H^+ exchange

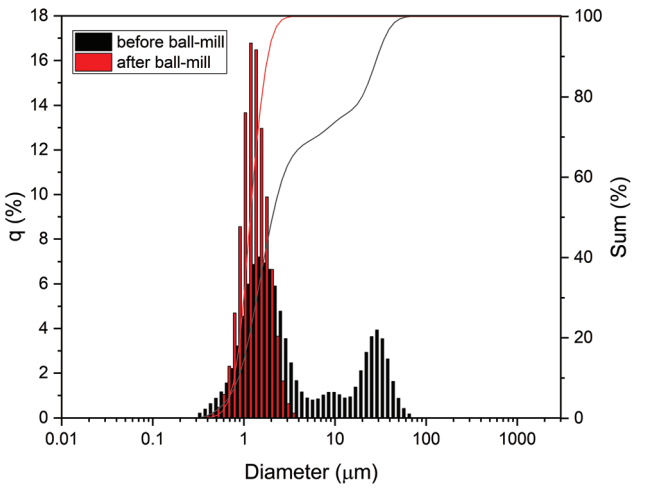

Fig. 2 PSD of LLZ:AlTa powder before and after ball-milling.

reaction with water and results in the increase of pH up to 11–12.[52–54]

$$Li_7La_3Zr_2O_{12} + xH_2O \rightarrow Li_{7-x}H_xLa_3Zr_2O_{12} + xLi^+ + xOH^- \quad (1)$$

A large amount of OH^- anions will be adsorbed on the surface of LLZ particle to provide the electrostatic repulsive force, which further stabilizes the suspension (details in ESI†). In our case, the pH value of the prepared slurry, due to the high solid loading, reached pH 12.5 directly after mixing LLZ:AlTa powder with the aqueous polymer solution. The rheological behavior of the prepared slurry was then investigated, which shows a shear thinning behavior (Fig. 3a) in the suitable range for tape casting. The high viscosity of the slurry at low shear rate will prevent the inhomogeneous sedimentation of ceramic particles during the drying step after casting. This is an important point to the process, because the drying of aqueous tapes takes much longer time than ethanol-based ones due to the slower evaporation rate of water. In industrial processing, however, the drying time can be reduced through application of heat below and/or over the tapes. The dried green tape, as shown in Fig. 3b, was soft and flexible, which can be easily cut into desired sizes and shapes for the subsequent sintering step. Through controlling the height of doctor blade, the thickness of green tapes can be varied from 60 to 140 μm. Although the slurry was prepared as foam free, the green tapes still exhibit certain porosities created by the evaporation of solvent. Therefore, it is necessary to laminate and compress the green tapes to increase their green density.

In the TG analysis of the green tape several steps with weight loss were observed (Fig. 3c). MS was applied to identify the source of each weight loss step. The MS curves corresponding to H_2O (m/z = 18) and CO_2 (m/z = 44) are presented in Fig. 3c as well. The remaining water in the green tapes starts to evaporate at around 50 °C. The weight loss at the temperatures between 200 and 620 °C is about 15%, which is close to the total organic content in the green tapes, indicating that all organic additives are burned out at this stage (debinding stage). The CO_2 evolution is observed between 650 and 900 °C, which can be assigned to the decomposition of Li_2CO_3 present on the surface of the LLZ:AlTa powder (as evident from Fig. S1†). No further weight loss was observed beyond 900 °C. For the final densification the tapes were sintered at a temperature of 1175 °C with 4 h dwell time, which was shown to be the optimum sintering temperature reported in our previous work.[50] The fresh sintered sheets of LLZ-air show a yellowish color, as shown in the inset of Fig. 4a. The sintered thin sheets have a thickness of ~150 μm the apparent density of approx. 90% (Fig. 4c). The yellowish color of LLZ-air can be attributed to a Li_2CO_3 layer on the surface, which can be seen clearly in the BSE-SEM image (Fig. 4a), showing a phase in dark color. This observation is in agreement with Li *et al.*[55] was observed. The presence of Li_2CO_3 is also detected in XRD pattern (Fig. 4d) showing diffraction peaks at 21° and 24° but with quite low intensity due to the bulk sensitivity of XRD. A surface sensitive Raman spectroscopy was used to confirm the existing of Li_2CO_3, which is indicated by the strong band at 1090 cm^{-1} originated from the CO_3^{2-} symmetric stretching vibration of Li_2CO_3 (Fig. 4e).[56] Since the Li_2CO_3 in the synthesized powder as well as the one in the green tapes formed during drying has been thermally decomposed during the sintering at elevated temperature according to the TG results, it is reasonable to suggest that this impurity layer was formed during the cooling process in ambient atmosphere.

The presence of the Li_2CO_3 passivation layer on the surface of sintered LLZ sheet is disadvantageous as it is known to increase the interfacial resistance between garnet and lithium metal.[57] Li_2CO_3 layer can be however removed by annealing in Ar.[58] After annealing in Ar, the obtained free-standing garnet solid electrolyte LLZ-Ar is partially transparent with color in white (shown in the inset of Fig. 4b), indicating the successful removal of the impurities. SEM image (Fig. 4b) reveals a clean surface of LLZ-Ar, and there are no diffraction peaks in XRD (Fig. 4d) or Raman bands (Fig. 4e) related to Li_2CO_3. ICP-OES reveals the final composition of the solid electrolyte LLZ-Ar close to the stoichiometric composition (Table S1†). It should be noted however that the freshly sintered tapes in our process

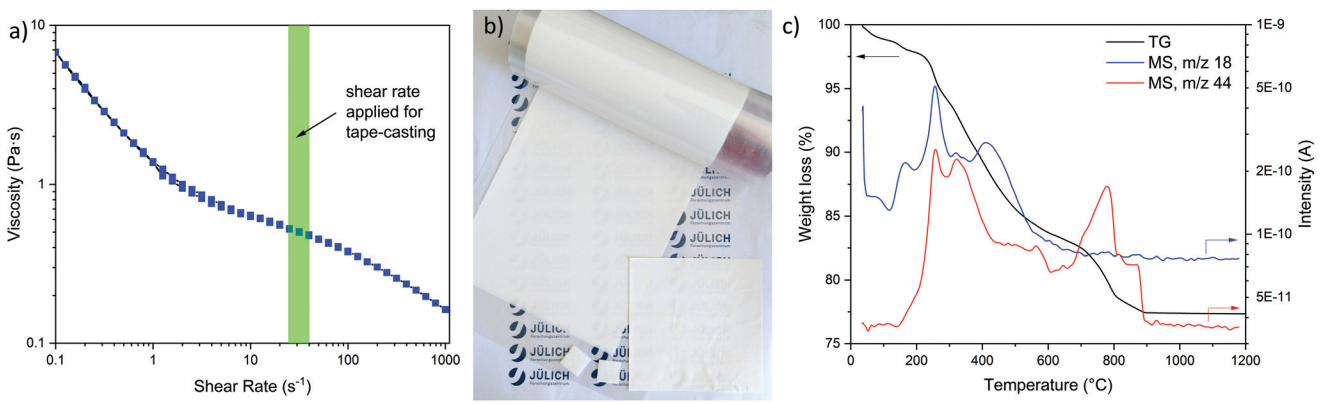

Fig. 3 (a) Viscosity *versus* shear rate curve of the prepared slurry for tape casting; (b) photograph of the green tapes (size of the small square tape: 1.5 cm × 1.5 cm; size of the large square tape: 9 cm × 9 cm); (c) TG with MS of green tape.

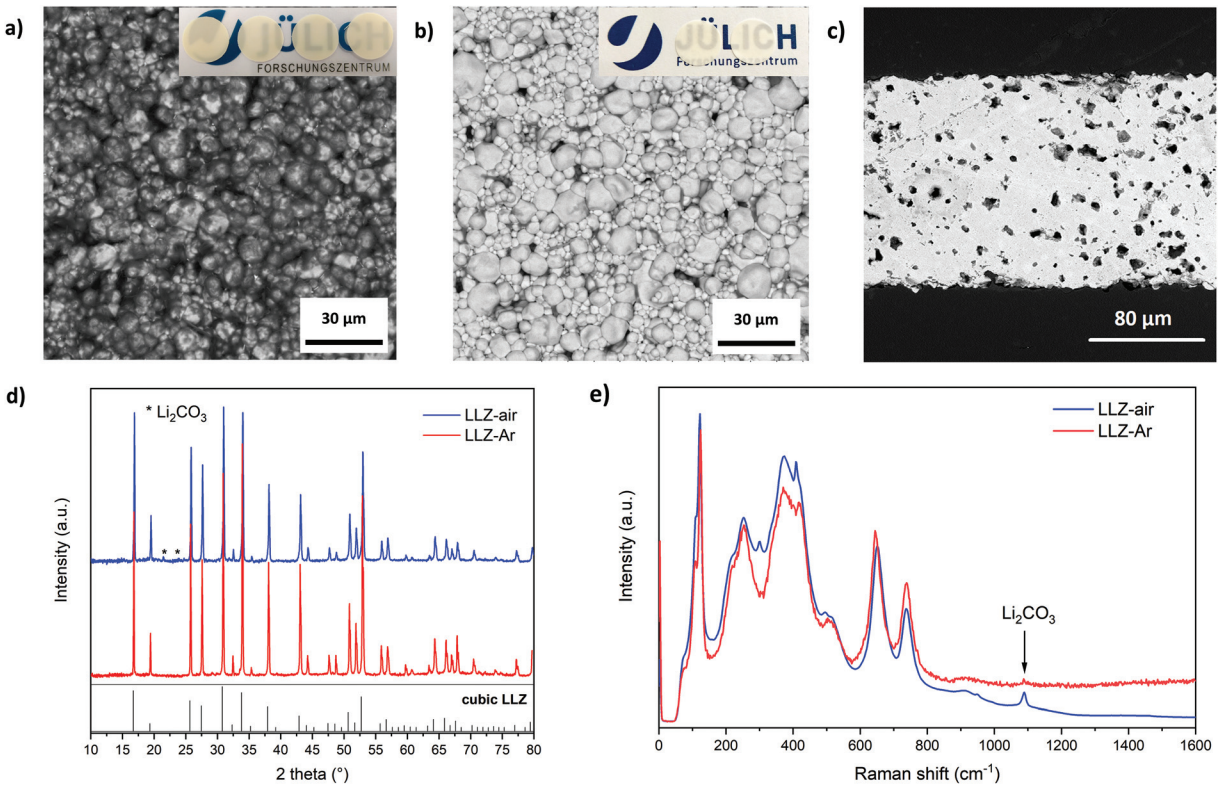

Fig. 4 (a) Surficial SEM image of LLZ-air (inset: photograph of LLZ-air, size: *ca.* 11 mm in diameter); (b) surficial SEM image LLZ-Ar (inset: photograph of LLZ-Ar, size: *ca.* 11 mm in diameter); (c) cross-sectional SEM image of LLZ-air; (d) XRD patterns of LLZ-air and LLZ-Ar; (e) Raman spectra of LLZ-air and LLZ-Ar.

are carbonate-free and the Li_2CO_3 layer is formed during the cooling step in ambient atmosphere. Therefore, an additional annealing step can be avoided by performing sintering in a dry room or switching the atmosphere during the cooling step.

Effect of water

To fully understand the effect of water in this developed aqueous processing for LLZ, the impact of the Li^+/H^+-exchange reaction was investigated. For that, we prepared samples to carry out ICP-OES and XRD measurements on all LLZ samples for each step of the whole fabrication procedure: (1) starting powder "LLZ:AlTa", (2) solid filtrated from water-based slurry "LLZ-slurry", (3) the green tape "LLZ-green", (4) the sintered "LLZ-air" and "LLZ-Ar". Lattice parameters for cubic LLZ were calculated from Rietveld refinement of the respective XRD data. The obtained results of elemental compositions from ICP-OES and lattice parameters as well as corresponding phase contents from Rietveld refinement are compiled in Table S1† and Table 3, respectively. The elemental analysis reveals severe Li loss for LLZ particles in "LLZ-slurry" by nearly one third when compared to the starting powder, indicating strong Li^+/H^+-exchange between garnet powder and the aqueous medium in slurry, which results in the dramatically increasing of pH value of the slurry up to 12.5. On the other hand, the Li loss in the sintered samples is related to the expected Li evaporation at high temperature. Li_2CO_3 is hardly to find in "LLZ-slurry" because the carbonate in pristine powder as well as LiOH (the product of Li^+/H^+-exchange) was dissolved in water and left in filtrate. The solid "LLZ-slurry" after such severe Li^+/H^+-exchange could hardly further form new carbonate when exposure to air. It should be mentioned that "LLZ slurry" is not a step involved in our aqueous tape-casting process and is demonstrated here only for the purpose of investigation on Li^+/H^+-exchange. In comparison we found an increasing portion of Li_2CO_3 in green tapes "LLZ-green", which can be attributed to the Li^+/H^+-exchange. These carbonates provide Li source for the Li-recovery in LLZ at elevated temperature that we will discuss later in this section. Interestingly, we found two cubic phases of LLZ in all samples after the Rietveld refinement. One of them has a smaller lattice parameter around 12.95 Å, noted as phase #1, and the other has a relatively larger lattice parameter over 13.00 Å, noted as phase #2. Quantitative phase analysis results at different steps showed that the ratio of phase #1 decreases with the increasing ratio of phase #2 when LLZ powder is immersed in water, whereas the phase #2 is almost completely converted into phase #1 upon sintering. Comparing the lattice parameters of both phases with literature data of Ta-substituted LLZ,[54] we can conclude that phase #1 is cubic phase LLZ stabilized by Ta-substitution without proton, while the phase #2 is stabilized by proton, in which the proton substitution leads to a lattice expansion. The observed reversibility of this

Table 3 Lattice parameters and phase analysis of LLZ samples from each step of fabrication procedure

	LLZ phase #1		LLZ phase #2		Li_2CO_3
	Lattice parameter [Å]	Weight percentage [%]	Lattice parameter [Å]	Weight percentage [%]	Weight percentage [%]
LLZ:AlTa	12.950(2)	83	12.99(6)	15	2
LLZ-slurry	12.965(3)	58	13.01(2)	42	0
LLZ-green[a]	12.97(1)	34	13.03(1)	62	3
LLZ-air	12.946(2)	92	12.98(9)	6	2
LLZ-Ar[b]	12.944(1)	95	12.98(6)	3	1

[a] Rest impurities in "LLZ-green": $La(OH)_3$ (1%). [b] Rest impurities in "LLZ-Ar": $La_2Zr_2O_7$ (<0.5%) and La_2O_3 (<0.5%).

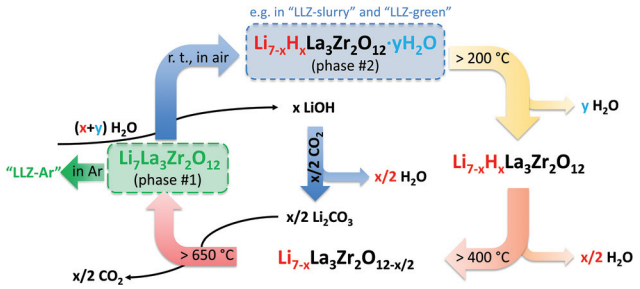

Fig. 5 Schematic representation of the reversible phase transition mechanism between pure LLZ and hydrated LLZ based on ref. 59. To simplify the expressions, Al and Ta are removed in this schematic.

phase transition of water-treated LLZ upon heating can be explained by the mechanism proposed by Larraz *et al.*[59] and a schematic representation thereof is shown in Fig. 5. Through the Li^+/H^+-exchange and the insertion of water molecules into LLZ structure, a hydrated cubic garnet is formed, which can be expressed as $Li_{7-x}H_xLa_3Zr_2O_{12}\cdot yH_2O$. This hydrated garnet losses the water of hydration between 200–250 °C to result in the cubic protonated garnet $Li_{7-x}H_xLa_3Zr_2O_{12}$, which further releases water between 400–450 °C giving rise to a cubic garnet with O-vacancy $Li_{7-x}La_3Zr_2O_{12-x/2}$. The latter reacts with Li_2CO_3 at around 700 °C to form stoichiometric cubic $Li_7La_3Zr_2O_{12}$. Our results clearly show that the garnet stoichiometry is recovered at the end, though it is hydrated and protonated at the beginning. The only two other reported works regarding aqueous processing of LLZ, extra LiOH was intentionally added to suppress the Li^+/H^+-exchange reaction.[40,60] However, our study clearly demonstrates that even without additional LiOH was added into slurry, the stoichiometric cubic LLZ can still be obtained after final heat treatment. Therefore, the water-based processing route we developed is feasible to obtain pure cubic garnet SEs.

Electrochemical characterization

The ionic conductivity of the "LLZ-Ar" sheets was determined by EIS measurement using a Li|LLZ-Ar|Li symmetric cell. The resulting Nyquist plot and its equivalent circuit are shown in Fig. 6a. In the equivalent circuit, parallel elements of resistor (R) and constant phase element (CPE) are used to fit semicircles, while an inductor (L) is added due to wiring. We can see two semicircles that represent the resistances originating from the LLZ-Ar at high frequency (corresponding capacitance 4.93×10^{-10} F) and the LLZ-Ar/Li-interface at low frequency (corresponding capacitance 3.94×10^{-5} F), respectively. The bulk and grain boundary conductivities in polycrystalline ceramics measured by EIS usually exhibit capacitances in 10^{-12} F and 10^{-11}–10^{-8} F range, respectively.[61] Thus for our measurements, we assign the high-frequency semicircle with a capacitance in 10^{-10} F to the grain boundary resistance of LLZ-Ar ($R2$), while the bulk resistance is presented by the serial resistance $R1$ at high frequency. Thus, the total ionic conductivity of LLZ-Ar is 0.15 mS cm^{-1} at room temperature (detailed calculation see ESI and Table S2†), which is comparable with reported garnet SEs fabricated by conventional (non-aqueous) tape-casting (Table 1). The sample-electrode interface usually exhibits a capacitance in the 10^{-7}–10^{-5} F range. Hence, the low-frequency semicircle with a capacitance in 10^{-5} F was attributed to the interfacial resistance between LLZ-Ar and Li metal.

For application in SSLBs or other advanced battery concepts, the SE must show broad electrochemical stability window. To characterize the electrochemical stability, the LLZ-Ar layers were assembled in a Li|LLZ-Ar|In cell and CV measurements were carried out with a two-electrode set-up using Li as both counter and reference electrode. In the CV shown in Fig. 6b, the reduction peak onset at 0.61 V *vs.* Li^+/Li can be assigned to the formation of Li–In alloy, while the corresponding oxidation peak onset at 0.62 V *vs.* Li^+/Li represents the de-alloying of Li from the formed Li–In alloy.[62] Another reduction peak near 0 V *vs.* Li^+/Li is the Li plating process together with subsequent non-redox Li diffusion into In forming the Li–In alloy. No other redox peaks are observed in the whole scan range, indicating electrochemical stability of the prepared SE. Meanwhile, the wide voltage window up to 5 V *vs.* Li^+/Li, *i.e.* 4.4 V *vs.* Li^+/Li–In allows the use of high-voltage cathode materials in SSLBs in the future. Nevertheless, other *operando* and *ex situ* characterization methods are still required to comprehensively determine the electrochemical stability window of the SE separator *versus* Li metal.[63,64]

To further practically investigate the Li-conducting behavior of the prepared SE, Li stripping/plating tests were carried out with stepwise increasing current density (from 5 to 30 μA cm^{-2} with increment of 5 μA cm^{-2} per step) first to determine the

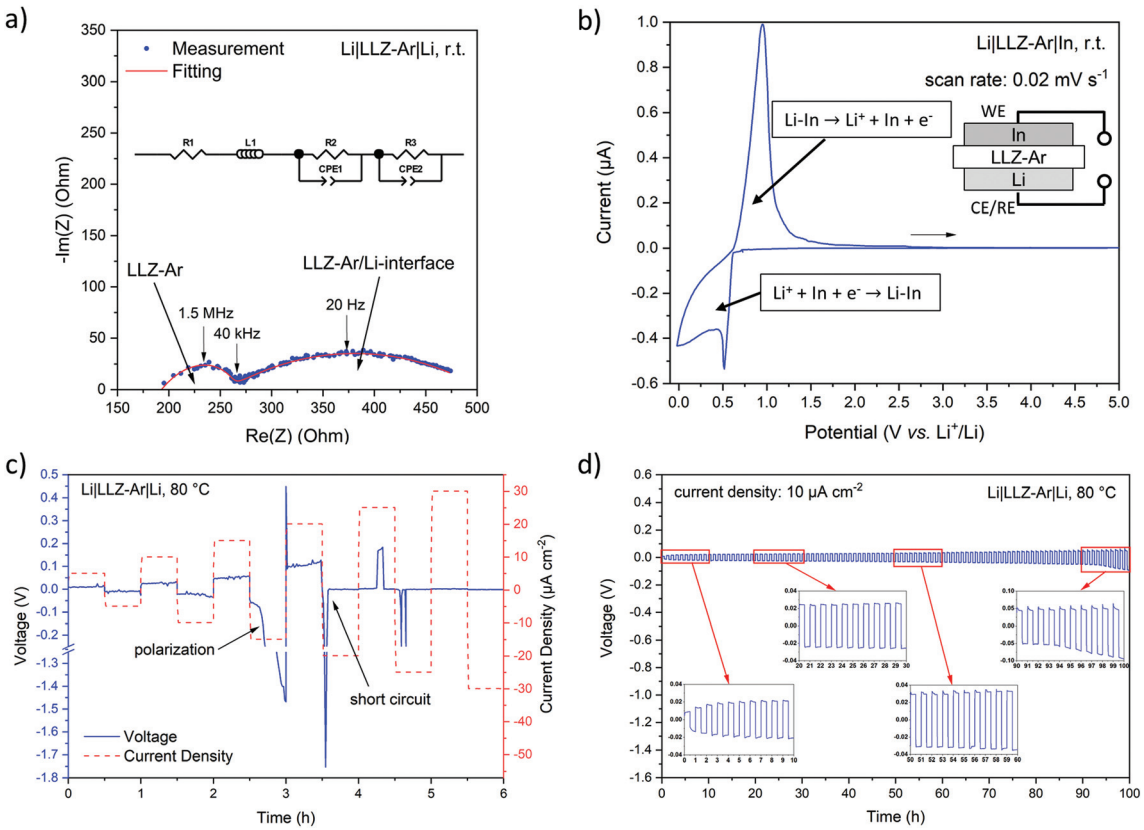

Fig. 6 (a) Nyquist plots of a Li|LLZ-Ar|Li symmetric cell measured at r.t. (inset shows the equivalent circuit for fitting, where R is resistor, L is inductor and CPE is constant phase element); (b) CV curve of a Li|LLZ-Ar|In cell measured at room temperature (inset schematically represents the test cell for CV with WE: working electrode, CE: counter electrode and RE: reference electrode); (c) voltage profile of a Li|LLZ-Ar|Li symmetric cell under variable current densities at 80 °C; (d) galvanostatic cycling of a Li|LLZ-Ar|Li symmetric cell at 10 μA cm^{-2} at 80 °C.

critical current density and later with a constant one (10 μA cm^{-2}) to study the long-term cycling performance. 80 °C was chosen as the operation temperature because of a faster Li diffusion in SE and a higher ductility of the Li metal anode at this temperature. In the voltage profile under variable current densities (Fig. 6c) we found that the Li|LLZ-Ar|Li symmetric cell can cycle steadily up to a current density of 15 μA cm^{-2} (with some polarization) whereas increasing the current density further to 20 μA cm^{-2} leads to a short circuit most likely caused by dendrite formation. Although this critical current density value is still far away from practical application and some reports show 1–2 orders of magnitude higher ones,[33,40] it is still in the range of reported operational current densities of ASSLBs with dense, free sintered garnet SE separators. It seems that the low Li self-diffusion in the Li metal results in poor contact between garnet and metal anode, leading to fast dendrite formation.[1,50,65] Therefore, a safe current density for the prepared SE was set to 10 μA cm^{-2}, which was then applied for the long-term cycling. The obtained cycling profile (Fig. 6d) shows the steady Li-conducting performance over 100 hours without short circuit, though we observed slightly increased voltages after 90 hours as a consequence of increasing Li/SE-interface resistance due to the roughness on the SE surface. Since we did not do any Li/SE-interface modification, the observed critical current density as well as the Li-stripping/plating performance could depend rather on the Li/SE-interface contact than on the conductivity of SE itself. The Li foils in these demonstrated cells were all attached by hand, which may lead to large difference in the Li/SE-interfacial resistance from one cell to another. To avoid this issue, it would be better to deposit Li onto the SE by for instance an evaporator.

Conclusions

We successfully developed a water-based tape-casting process using eco-friendly binders to fabricate thin free-standing garnet solid electrolyte (SE). We showed that the occurring Li^+/H^+-exchange reaction is completely reversible in our process and enables the formation of stoichiometric Ta- and Al-substituted LLZ with cubic phase. The obtained garnet SEs shows a total ionic conductivity of 0.15 mS cm^{-1} at room temperature and is (electro-)chemically stable against lithium metal within the boundaries of the experiment. Therefore, our developed water-based tape-casting process paves a green way to fabricate

free-standing garnet SE separator, which is suitable to be employed in SSLBs with SE-supported configuration or in other advanced Li-battery having Li-metal anodes. Further work needs to be done on modification of SE/Li-interface to achieve a higher applicable current density and better long-term cycling performance.

Author contributions

R.Y. conducted experiments, analyzed data and wrote the manuscript; C.-L.T. conducted Raman measurements and gave discussion on material synthesis and characterizations; M.I. and S.S. gave discussion on electrochemical characterizations and analysis; M.R. and E.D. gave discussion on tape casting and sintering of LLZ thin sheets; Y.-J.S. conducted the Rietveld refinement on XRD data; E.F. and M.F. initiated the idea, supervised the work and managed the funding project. All authors revised the manuscript.

Conflicts of interest

There are no conflicts to declare.

Acknowledgements

This work is supported by the Ministry of Economic Affairs, Innovation, Digitalization and Energy of the state North Rhine-Westphalia in the project 'GrEEn' (project number: 313-W044B). The authors would like to thank Philipp Hecker and Grit Häuschen for the helps in LLZ:AlTa powder synthesis, Andrea Hilgers for the PSD and rheology tests, Marie-Theres Gerhards for the thermal analysis, Volker Bader for the heat treatments and Volker Nischwitz for the ICP-OES measurements.

References

1 C. Wang, K. Fu, S. P. Kammampata, D. W. McOwen, A. J. Samson, L. Zhang, G. T. Hitz, A. M. Nolan, E. D. Wachsman, Y. Mo, V. Thangadurai and L. Hu, *Chem. Rev.*, 2020, **120**, 4257–4300.
2 Y. Ding, Z. P. Cano, A. Yu, J. Lu and Z. Chen, *Electrochem. Energy Rev.*, 2019, **2**, 1–28.
3 T. Placke, R. Kloepsch, S. Dühnen and M. Winter, *J. Solid State Electrochem.*, 2017, **21**, 1939–1964.
4 V. Etacheri, R. Marom, R. Elazari, G. Salitra and D. Aurbach, *Energy Environ. Sci.*, 2011, **4**, 3243–3262.
5 B. Dunn, H. Kamath and J. M. Tarascon, *Science*, 2011, **334**, 928–935.
6 Z. G. Yang, J. L. Zhang, M. C. W. Kintner-Meyer, X. C. Lu, D. W. Choi, J. P. Lemmon and J. Liu, *Chem. Rev.*, 2011, **111**, 3577–3613.
7 M. Armand and J. M. Tarascon, *Nature*, 2008, **451**, 652–657.
8 J. Janek and W. G. Zeier, *Nat. Energy*, 2016, **1**, 16141.
9 A. Manthiram, X. W. Yu and S. F. Wang, *Nat. Rev. Mater.*, 2017, **2**, 16103.
10 Z. H. Gao, H. B. Sun, L. Fu, F. L. Ye, Y. Zhang, W. Luo and Y. H. Huang, *Adv. Mater.*, 2018, **30**, 1705702.
11 K. Takada, *J. Power Sources*, 2018, **394**, 74–85.
12 N. Zhao, W. Khokhar, Z. Bi, C. Shi, X. Guo, L.-Z. Fan and C.-W. Nan, *Joule*, 2019, **3**, 1190–1199.
13 J. Yue, M. Yan, Y.-X. Yin and Y.-G. Guo, *Adv. Funct. Mater.*, 2018, **28**, 1707533.
14 N. Imanishi and O. Yamamoto, *Mater. Today Adv.*, 2019, **4**, 100031.
15 A. J. Samson, K. Hofstetter, S. Bag and V. Thangadurai, *Energy Environ. Sci.*, 2019, **12**, 2957–2975.
16 Y. Li, J.-T. Han, C.-A. Wang, H. Xie and J. B. Goodenough, *J. Mater. Chem.*, 2012, **22**, 15357–15361.
17 V. Thangadurai, S. Narayanan and D. Pinzaru, *Chem. Soc. Rev.*, 2014, **43**, 4714–4727.
18 L. J. Miara, W. D. Richards, Y. E. Wang and G. Ceder, *Chem. Mater.*, 2015, **27**, 4040–4047.
19 P. Albertus, S. Babinec, S. Litzelman and A. Newman, *Nat. Energy*, 2018, **3**, 16–21.
20 S. Ramakumar, C. Deviannapoorani, L. Dhivya, L. S. Shankar and R. Murugan, *Prog. Mater. Sci.*, 2017, **88**, 325–411.
21 R. Murugan, V. Thangadurai and W. Weppner, *Angew. Chem., Int. Ed.*, 2007, **46**, 7778–7781.
22 K. Kerman, A. Luntz, V. Viswanathan, Y. M. Chiang and Z. B. Chen, *J. Electrochem. Soc.*, 2017, **164**, A1731–A1744.
23 J. Schnell, T. Gunther, T. Knoche, C. Vieider, L. Kohler, A. Just, M. Keller, S. Passerini and G. Reinhart, *J. Power Sources*, 2018, **382**, 160–175.
24 J. Schnell, F. Tietz, C. Singer, A. Hofer, N. Billot and G. Reinhart, *Energy Environ. Sci.*, 2019, **12**, 1818–1833.
25 J. F. Nonemacher, C. Huter, H. Zheng, J. Malzbender, M. Kruger, R. Spatschek and M. Finsterbusch, *Solid State Ionics*, 2018, **321**, 126–134.
26 D. Hotza and P. Greil, *Mater. Sci. Eng., A*, 1995, **202**, 206–217.
27 M. Jabbari, R. Bulatova, A. I. Y. Tok, C. R. H. Bahl, E. Mitsoulis and J. H. Hattel, *Mater. Sci. Eng., B*, 2016, **212**, 39–61.
28 R. K. Nishihora, P. L. Rachadel, M. G. N. Quadri and D. Hotza, *J. Eur. Ceram. Soc.*, 2018, **38**, 988–1001.
29 E. Y. Yi, W. M. Wang, J. Kieffer and R. M. Laine, *J. Mater. Chem. A*, 2016, **4**, 12947–12954.
30 E. Y. Yi, W. M. Wang, J. Kieffer and R. M. Laine, *J. Power Sources*, 2017, **352**, 156–164.
31 K. Fu, Y. H. Gong, G. T. Hitz, D. W. McOwen, Y. J. Li, S. M. Xu, Y. Wen, L. Zhang, C. W. Wang, G. Pastel, J. Q. Dai, B. Y. Liu, H. Xie, Y. G. Yao, E. D. Wachsman and L. B. Hu, *Energy Environ. Sci.*, 2017, **10**, 1568–1575.
32 B. Liu, L. Zhang, S. Xu, D. W. McOwen, Y. Gong, C. Yang, G. R. Pastel, H. Xie, K. Fu, J. Dai, C. Chen, E. D. Wachsman and L. Hu, *Energy Storage Mater.*, 2018, **14**, 376–382.

33 G. T. Hitz, D. W. McOwen, L. Zhang, Z. H. Ma, Z. Z. Fu, Y. Wen, Y. H. Gong, J. Q. Dai, T. R. Hamann, L. B. Hu and E. D. Wachsman, *Mater. Today*, 2019, **22**, 50–57.
34 R. A. Jonson and P. J. McGinn, *Solid State Ionics*, 2018, **323**, 49–55.
35 E. Hanc, W. Zajac, L. Lu, B. G. Yan, M. Kotobuki, M. Ziabka and J. Molenda, *J. Solid State Chem.*, 2017, **248**, 51–60.
36 L. Cheng, S. Lyer, W. Gardner, T. Holme, S. Li, C.-c. Chao, N. Donnelly and A. Allenic, *United States Pat*, US9966630B2, 2018.
37 K. N. Gao, M. H. He, Y. Q. Li, Y. P. Zhang, J. Gao, X. X. Li, Z. H. Cui, Z. L. Zhan and T. Zhang, *J. Alloys Compd.*, 2019, **791**, 923–928.
38 Y. Jin and P. J. McGinn, *J. Power Sources*, 2013, **239**, 326–331.
39 M. E. Badding, Y. Chen, X. Huang, C. Liu, X. Liu, Y. A. Lu, Z. Song, Z. Wen, T. Xiu and N. M. Zink, *United States Pat*, US20180301754A1, 2018.
40 X. Peng, X. K. Zhang, K. Huang, S. P. Song and Y. Xiang, *ChemElectroChem*, 2019, **6**, 2945–2948.
41 D. Bresser, D. Buchholz, A. Moretti, A. Varzi and S. Passerini, *Energy Environ. Sci.*, 2018, **11**, 3096–3127.
42 N. Böckenfeld, S. S. Jeong, M. Winter, S. Passerini and A. Balducci, *J. Power Sources*, 2013, **221**, 14–20.
43 C. Y. Yang, C. H. Cheng, S. M. Ho, J. C. Chen and W. M. Hurng, *J. Power Sources*, 1997, **68**, 440–442.
44 W. Porcher, B. Lestriez, S. Jouanneau and D. Guyomard, *J. Electrochem. Soc.*, 2009, **156**, A133–A144.
45 Z. P. Cai, Y. Liang, W. S. Li, L. D. Xing and Y. H. Liao, *J. Power Sources*, 2009, **189**, 547–551.
46 N. S. Hochgatterer, M. R. Schweiger, S. Koller, P. R. Raimann, T. Wöhrle, C. Wurm and M. Winter, *Electrochem. Solid-State Lett.*, 2008, **11**, A76–A80.
47 J.-H. Lee, U. Paik, V. A. Hackley and Y.-M. Choi, *J. Electrochem. Soc.*, 2005, **152**, A1763–A1769.
48 J. Xu, S.-L. Chou, Q.-f. Gu, H.-K. Liu and S.-X. Dou, *J. Power Sources*, 2013, **225**, 172–178.
49 C. A. Geiger, E. Alekseev, B. Lazic, M. Fisch, T. Armbruster, R. Langner, M. Fechtelkord, N. Kim, T. Pettke and W. Weppner, *Inorg. Chem.*, 2011, **50**, 1089–1097.
50 C.-L. Tsai, Q. Ma, C. Dellen, S. Lobe, F. Vondahlen, A. Windmüller, D. Grüner, H. Zheng, S. Uhlenbruck, M. Finsterbusch, F. Tietz, D. Fattakhova-Rohlfing, H. P. Buchkremer and O. Guillon, *Sustainable Energy Fuels*, 2019, **3**, 280–291.
51 P. L. Nasatto, F. Pignon, J. L. M. Silveira, M. E. R. Duarte, M. D. Noseda and M. Rinaudo, *Polymers*, 2015, **7**, 777–803.
52 C. Liu, K. Rui, C. Shen, M. E. Badding, G. X. Zhang and Z. Y. Wen, *J. Power Sources*, 2015, **282**, 286–293.
53 C. Ma, E. Rangasamy, C. Liang, J. Sakamoto, K. L. More and M. Chi, *Angew. Chem., Int. Ed.*, 2015, **54**, 1063–1063.
54 Z. F. Yow, Y. L. Oh, W. Y. Gu, R. P. Rao and S. Adams, *Solid State Ionics*, 2016, **292**, 122–129.
55 Y. Li, X. Chen, A. Dolocan, Z. Cui, S. Xin, L. Xue, H. Xu, K. Park and J. B. Goodenough, *J. Am. Chem. Soc.*, 2018, **140**, 6448–6455.
56 P. Pasierb, S. Komornicki, M. Rokita and M. Rękas, *J. Mol. Struct.*, 2001, **596**, 151–156.
57 L. Cheng, E. J. Crumlin, W. Chen, R. Qiao, H. Hou, S. F. Lux, V. Zorba, R. Russo, R. Kostecki, Z. Liu, K. Persson, W. Yang, J. Cabana, T. Richardson, G. Chen and M. Doeff, *Phys. Chem. Chem. Phys.*, 2014, **16**, 18294–18300.
58 L. Cheng, M. Liu, A. Mehta, H. Xin, F. Lin, K. Persson, G. Chen, E. J. Crumlin and M. Doeff, *ACS Appl. Energy Mater.*, 2018, **1**, 7244–7252.
59 G. Larraz, A. Orera and M. L. Sanjuan, *J. Mater. Chem. A*, 2013, **1**, 11419–11428.
60 X. Huang, Y. Lu, J. Tin, S. Gu, T. P. Xiu, Z. Song, M. E. Badding and Z. Y. Wen, *ACS Appl. Mater. Interfaces*, 2018, **10**, 17147–17155.
61 I. M. Hodge, M. D. Ingram and A. R. West, *J. Electroanal. Chem. Interfacial Electrochem.*, 1976, **74**, 125–143.
62 A. L. Santhosha, L. Medenbach, J. R. Buchheim and P. Adelhelm, *Batteries Supercaps*, 2019, **2**, 524–529.
63 F. Han, Y. Zhu, X. He, Y. Mo and C. Wang, *Adv. Energy Mater.*, 2016, **6**, 1501590.
64 T. Thompson, S. Yu, L. Williams, R. D. Schmidt, R. Garcia-Mendez, J. Wolfenstine, J. L. Allen, E. Kioupakis, D. J. Siegel and J. Sakamoto, *ACS Energy Lett.*, 2017, **2**, 462–468.
65 T. Krauskopf, H. Hartmann, W. G. Zeier and J. Janek, *ACS Appl. Mater. Interfaces*, 2019, **11**, 14463–14477.